

# Effect of electrolyte on the microstructure and yielding of aqueous dispersions of colloidal clay

Samim Ali\* and Ranjini Bandyopadhyay†

*Raman Research Institute, C. V. Raman Avenue,  
Sadashivanagar, Bangalore 560080, India*

## Abstract

Na-montmorillonite is a natural clay mineral and is available in abundance in nature. The aqueous dispersions of charged and anisotropic platelets of this mineral exhibit non-ergodic kinetically arrested states ranging from soft glassy phases dominated by interparticle repulsions to colloidal gels stabilized by salt induced attractive interactions. When the salt concentration in the dispersing medium is varied systematically, viscoelasticity and yield stress of the dispersion show non-monotonic behavior at a critical salt concentration, thus signifying a morphological change in the dispersion microstructures. We directly visualize the microscopic structures of these kinetically arrested phases using cryogenic scanning electron microscopy. We observe the existence of honeycomb-like network morphologies for a wide range of salt concentrations. The transition of the gel morphology, dominated by overlapping coin (OC) and house of cards (HoC) associations of clay particles at low salt concentrations to a new network structure dominated by face-face coagulation of platelets, is observed across the critical salt concentration. We further assess the stability of these gels under gravity using electroacoustics. This study, performed for concentrated clay dispersions for a wide concentration range of externally added salt, is useful in our understanding of many geophysical phenomena that involve the salt induced aggregation of natural clay minerals.

---

\*Electronic address: samim@rri.res.in

†Electronic address: ranjini@rri.res.in

## I. INTRODUCTION

Aqueous dispersions of smectite clay minerals have been investigated extensively during the last decade to understand their rich phase behaviors [1, 2], aging dynamics [3–7] and unusual flow properties [8, 9]. The bulk properties of these dispersions originate from the complex self organization of charged anisotropic clay platelets [10], which leads to various phases such as gels, glasses [11], empty liquids, equilibrium gels [12] and nematic liquid crystals [13]. These phases and their bulk behaviors can easily be realized by tuning the colloidal interactions externally. This has led to widespread applications of these clay minerals as rheological modifiers and stabilizers in paints [14], well bore drilling [15], cosmetics [16], pharmaceuticals [16], agrochemicals and nanocomposites [17].

The charged anisotropic platelets of the Na-montmorillonite clay mineral used in this work are naturally occurring flexible nanosheets [18]. The platelets are highly polydisperse in their lateral sizes and shapes. The surfaces of these platelets have negative charges while the edges have pH dependent positive charges. In aqueous dispersions, the clay platelets are surrounded by hydrated  $\text{Na}^+$  counterions that form anisotropic electric double layers (EDL) around the platelets. Due to high concentration of negative charges on their basal surfaces, there is a small amount of spill-over of the negative potential onto the positively charged edges at  $\text{pH} > 7$  [19–21]. Due to the presence of the anisotropic EDL, the effective excluded volume of each platelet is much higher than its geometrical volume. The interaction potential between these platelets in dilute samples is usually represented by the DLVO theory [22] and depends on the mutual separation, the relative orientations and the charge distribution on the platelets. Thus, the formation of kinetically arrested phases such as soft glasses and gels in the dispersions can be controlled by changing clay mineral concentration, salt concentration and pH of the medium [1]. The rheological and stability properties of these disordered phases are directly related to the microscopic arrangements of the platelets in the dispersions. In the glassy phase, the interactions between platelets are dominated by screened Coulomb repulsions and the viscoelasticity and yielding behaviors originate from the caging of each platelet by its neighbors [23]. The gel phase, on the other hand, is a volume spanning network structure in which two platelets are connected by an attractive bond, with the strengths of the bonds determining their viscoelasticity and yielding behavior.

The nature of platelet association for attractive bond formation, and therefore the origin of the observed rheological behavior of Na-montmorillonite gels, have been widely debated in the literature [24–27]. Based on the DLVO theory and rheological measurements in dispersions of low platelet concentrations, it was predicted that at low salt concentration and in a dispersing medium of  $\text{pH} < 7$ , attractive bond formation occurs through the association of the negative faces of the platelets with their positive edges. On the other hand, bond formation through edge-face, face-face and edge-edge interactions are predicted at varying salt concentrations in a dispersing medium of  $\text{pH} > 7$  [28, 29]. The coagulation process becomes more complicated with increasing platelet concentration in the presence of salt and a house of cards (HoC) structure is frequently invoked to explain the nature of gel networks [30–35]. Surprisingly, the experimental evidence of such predicted microstructures is very limited. There have been some studies to visualize the underlying microscopic structures using scanning electron microscopy (SEM) [36] and transmission X-ray microscopy (TXM) [27, 37] for different conditions of sample preparation. These studies confirm the existence of either edge-edge or face-face microscopic configurations of platelets in the presence of salt. However, these studies do not systematically investigate the variation of the microscopic structures, and their influence on the strength and stability of clay gels, with changing salt concentration.

In this article, we address this issue by studying the rheology, stability properties and associated microstructures of 5% w/v Na-montmorillonite dispersions at their natural pH values after systematically varying the externally added salt concentration from 10 mM to 800 mM. We find that the viscoelastic moduli and the yield stress of arrested phases (gels) in the dispersion increase upto a peak value at a critical salt concentration and subsequently decrease due to the progressive increase in salt induced interparticle attractive interactions. The microscopic association of the platelets in gels with varying salt concentration is directly visualized using cryogenic scanning electron microscope (cryo-SEM). This shows a transition of the gel morphology, dominated by overlapping coin (OC) and house of cards (HoC) associations of clay particles to a new network structure dominated by face-face coagulation of platelets, across the critical salt concentration. The variation of the strength of the gels estimated from the rheological measurements is then interpreted in terms of the observed microstructures and changes in gel morphology. The influence of the morphology on the stability of the gels under gravity is further assessed using electroacoustics.

Besides their obvious rheological importance [18], clay colloids in aqueous dispersions have been studied extensively for their aging properties [38, 39]. The structure, dynamics and rheology of clay in water with and without salt have been widely debated [8, 26, 27]. Our present results, obtained for clay dispersions with a wide range of salt concentrations, will be useful to understand and predict many geophysical phenomena such as land slides, and the formation of river deltas and quicksand [40, 41] that are directly or indirectly related to the salt induced association of natural clay colloids.

## II. EXPERIMENTAL SECTION

### A. Material Structure

We use Na-montmorillonite of CEC value 145 meq/100g procured from Nanocor Inc [42]. A unit layer of this mineral is comprised of 2:1 layered phyllosilicate [43, 44]. The general formula is  $\text{Na}_x^+[(\text{Al}_{2-y}\text{Mg}_y)\text{Si}_4\text{O}_{10}(\text{OH})\cdot n\text{H}_2\text{O}]^-$  [18]. Each unit layer, also known as a platelet, consists of an aluminum octahedral sheet sandwiched between two tetrahedral silica sheets. The thickness of a platelet is around 1 nm. The lateral size of these platelets may vary from tens of nanometers to a few micrometers. In dry form, several platelets form a stack, known as a tactoid, with intercalated  $\text{Na}^+$  counterions. In aqueous dispersions, the  $\text{Na}^+$  ions get hydrated due to the absorption of water molecules in the intratactoid spaces. As a result, tactoids slowly swell and exfoliate, producing laminar flexible platelets with electric double layers (EDLs) on their surfaces [45–48]. The exfoliated platelets are highly irregular in shape and size (shown in a representative SEM micrograph in Fig. S1 of the ESI†). An average lateral size of 450 nm is calculated from the SEM micrographs (Fig. S2, ESI†).

### B. Sample preparation

The Na-montmorillonite powder is baked for 24 hours in an oven kept at a temperature of 120°C to remove moisture. A stock dispersion of 8% w/v is then prepared by dispersing the dry powder in highly deionized Milli-Q water under vigorous stirring conditions using a magnetic stirrer. The dispersion is homogenized by stirring it for three hours and then stored in a sealed polypropylene bottle for seven days. The stock dispersion is next used to prepare

5% w/v clay dispersions with different ionic strengths by adding predetermined quantities of NaCl solutions. The mixture of clay and salt solution is next stirred for three hours using a magnetic stirrer. The resultant dispersions are kept in vacuum for two minutes to remove air bubbles trapped in the viscous medium. Samples with different salt concentrations,  $C_s$ , are then stored for four days in sealed glass vials before using them for rheological measurements, cryo-SEM imaging and electroacoustic measurements. The pH of these dispersions are maintained at their natural values. The pH measurements are done using a CyberScan Eutech electrode (Model-ECFG7252001B) at a temperature of 25°C. The addition of salt leads to a slight decrease in the pH value of the dispersion and has been shown in Fig. S3 of the ESI†. It is seen that the pH of the dispersion always remains above 8.8 in the salt concentration range investigated here.

### C. Experimental setups and measurements

#### Cryogenic scanning electron microscopy (cryo-SEM):

For cryo-SEM characterization, shear melted samples with different salt concentrations are loaded by a syringe in capillary tubes (procured from Hampton Research, USA) of bore size 1 mm. The ends of the capillaries are then quickly sealed. Samples are then kept in an undisturbed condition for 48 hours. A home made sample holder is used for holding the sample capillaries. The samples are then vitrified using liquid nitrogen slush of temperature  $-200^\circ\text{C}$ . The vitrified samples are then fractured, sublimated for 12 mins at a temperature  $-90^\circ\text{C}$  and coated with a thin layer of platinum at a temperature  $-150^\circ\text{C}$  in vacuum using a cryotransfer system (PP3000T from Quorum Technologies). The imaging of these samples is then performed using a field effect scanning electron microscope (FESEM) from Carl Zeiss at an electron beam strength of 2 KeV.

#### Rheology:

Rheological measurements are performed by an Anton Paar MCR 501 rheometer working in a stress-controlled oscillatory mode. For each rheological experiment, a couette geometry is filled carefully with 4.7 ml of sample using a syringe. The filling process partially rejuvenates the sample. The free surface of the sample is covered with a thin layer of silicon oil of viscosity 5 cSt to prevent evaporation of water. A well defined experimental protocol, as shown in the inset of Fig. S4 of the ESI†, is used for all the measurements. After filling the

measurement geometry, the samples are shear rejuvenated by applying a large oscillatory stress of amplitude 50 Pa with an angular frequency of 6 rad/s. The application of this high shear stress liquifies the samples, leading to zero elastic modulus  $G'$  and very small values of viscous modulus  $G''$  (Fig. S4 of the ESI†). The samples are left to evolve for three hours after cessation of the shear melting process at age  $t_w = 0$ . During this period, the dispersions undergo a spontaneous phase transition from a liquid-like state to a kinetically arrested state, with the viscoelastic moduli evolving continuously with age  $t_w$  (Fig. S5, ESI†). After  $t_w = 3$  hours, a strain amplitude sweep test is carried out by varying strain amplitude,  $\gamma$ , in the range of 0.1 – 100% at a constant angular frequency of 6 rad/s (inset of Fig. S4 of the ESI†). All experiments reported here are carried out at a temperature of 25°C.

#### **Electroacoustics measurements:**

A cylindrical electroacoustic probe supplied by Dispersion Technology Inc is used to monitor the stability of clay dispersions under gravity. Details of the probe can be found in [49]. The ultrasound transducer in the probe is co-axially placed and then insulated from the outer metal body. The sedimentation setup using this probe is shown in Fig. S6 of the ESI†. In this setup, the front flat surface of the probe touches the top surface of the dispersion column. A very thin layer of silicon oil of viscosity 5 cSt (at 20°C) is placed between the probe and the dispersion. This keeps the sample from sticking to the flat surface of the probe. When the transducer launches a low power (10 mW) nondestructive plane ultrasound wave of frequency 3 MHz along the height of the sample, it induces small oscillating dipole moments in the EDLs of the clay platelets suspended in the dispersion. The electric field, generated from these induced dipoles, in turn, induces a current known as the colloidal vibration current ( $I_{CVI}$ ) in the receiving transducer circuit of the probe. If the dispersion contains salt, the transducer simultaneously detects an ionic vibration current ( $I_{IVI}$ ) which arises due to the relative motion between the two ion species of the salt. In this case, the total electroacoustic signal ( $I_{TVI}$ ) is a vector sum of  $I_{CVI}$  and  $I_{IVI}$ . The value of  $I_{TVI}$  measured in this setup is very sensitive to the distance of the clay particles comprising the gel from the measuring transducer [48]. Thus any shrinkage or settling of the gels will lead to a change in the measured values of  $I_{TVI}$ .

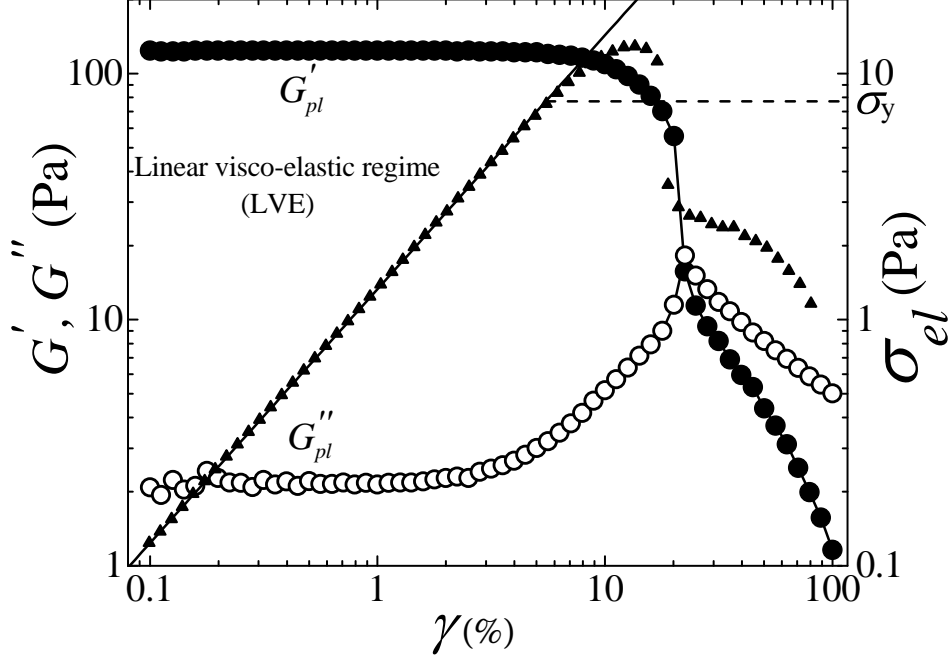


FIG. 1: Variation of elastic modulus  $G'$  ( $\bullet$ ), viscous modulus  $G''$  ( $\circ$ ) and elastic stress,  $\sigma_{el} = G'\gamma$  ( $\blacktriangle$ ) with strain amplitude,  $\gamma$ , for 5% w/v Na-montmorillonite with 20 mM added salt at  $t_w = 3$  hrs. The solid line is a linear fit to the  $\sigma_{el}$  vs  $\gamma$  data. The value of  $\sigma_y$  is shown by the horizontal dashed line.

### III. RESULTS AND DISCUSSION

The bulk mechanical behavior of Na-montmorillonite dispersions, with varying salt concentration  $C_s$ , is measured by performing strain amplitude sweep tests. Fig. 1 shows representative data of a strain amplitude sweep experiment at an angular frequency of 6 rad/s for a 5% w/v clay dispersion with  $C_s = 20$  mM at  $t_w = 3$  hrs. At small values of applied strain ( $\gamma$ ), i.e., in the linear viscoelastic (LVE) regime,  $G' > G''$ , with both the moduli being independent of strain amplitudes. The plateau values of  $G'$  and  $G''$  are designated by  $G'_{pl}$  and  $G''_{pl}$  respectively. On further increase in  $\gamma$ , the sample starts yielding due to the irreversible rearrangement of Na-montmorillonite platelets. In this nonlinear regime,  $G'$  decreases monotonically while  $G''$  reaches a peak at the point of crossover between  $G'$  and  $G''$ . Finally, at very high strains, the sample exhibits fluid-like behavior which is indicated

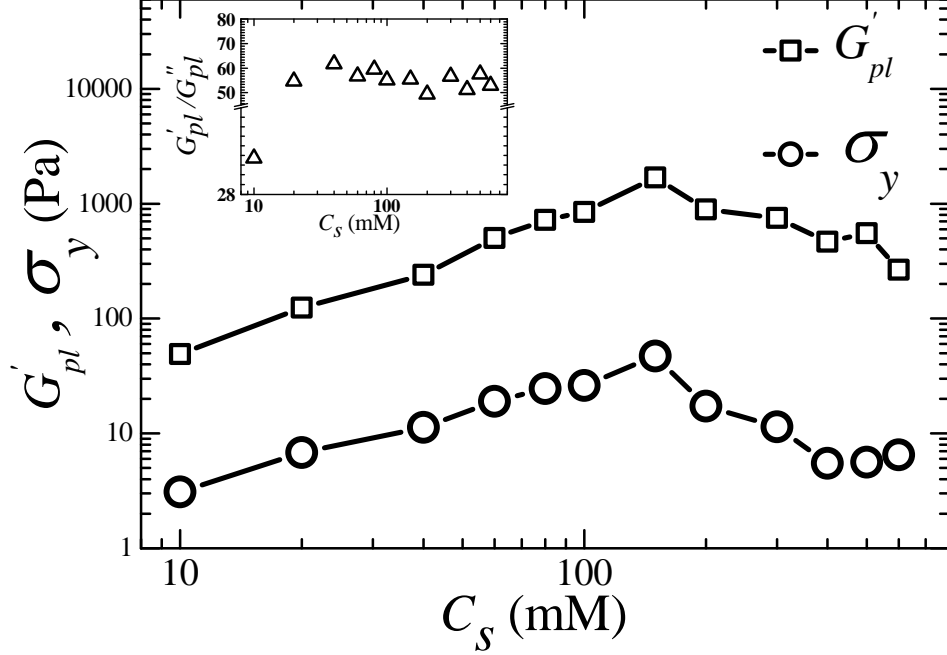


FIG. 2: Variation of plateau value of elastic modulus  $G'_{pl}$  ( $\square$ ) and dynamic yield stress  $\sigma_y$  ( $\circ$ ) with increasing salt concentration  $C_s$ . The inset shows the change in ratio of viscoelastic moduli  $G'_{pl}/G''_{pl}$  ( $\triangle$ ), measured in the linear viscoelastic regime, versus  $C_s$ .

by  $G'' > G'$ . Similar behavior of the stress moduli under high applied strains in the nonlinear regime was also observed previously in simulation and experimental studies [50, 51]. The dynamic yield stress,  $\sigma_y$  (indicated by horizontal dashed line in Fig. 1), is calculated from the strain amplitude sweep data following the method described by Laurati *et al.* [51]. In this method, the elastic stress  $\sigma_{el} = G'\gamma$  ( $\blacktriangle$  in Fig. 1) is plotted versus  $\gamma$ , which helps to separate the contribution of the viscous stress from the total stress. At low  $\gamma$  values, the elastic stress vs strain data is fitted to  $\sigma_{el} = G'\gamma$ . The value of  $\sigma_y$  is defined as the magnitude of  $\sigma_{el}$  at which the measured value of  $\sigma_{el}$  starts deviating from the theoretically calculated value. For the sample in Fig. 1, dynamical yield stress  $\sigma_y = 6.8$  Pa is calculated.

The variations of  $G'_{pl}$  and  $\sigma_y$  with varying salt concentration  $C_s$  are shown in Fig. 2. Both the quantities increase monotonically with  $C_s$  upto  $C_s \approx 150$  mM before they decrease with further addition of salt. The inset of Fig. 2 shows that  $G'_{pl}$  is approximately sixty times higher than  $G''_{pl}$  for samples with  $C_s > 10$  mM. This indicates that the dispersions are



essentially elastic in the linear viscoelastic regime, even though the strength of the underlying microstructures of the dispersions decreases for  $C_s > 150$  mM. The observations in Fig. 2 therefore indicate a transition in the sample morphology at  $C_s = 150$  mM.

We next investigate the salt induced morphological changes of Na-montmorillonite gels using cryo-SEM. Fig. 3 shows representative cryo-SEM micrographs of 5% w/v Na-montmorillonite gels with  $C_s$  varying in the range 10-500 mM. Honeycomb-like three dimensional network structures, with a systematic change in morphology and sizes of the polydisperse pores (voids left after sublimating the water molecules during the cryo-SEM sample preparation step), can be observed in all these samples. The branches of the gel networks observed here are thicker than the thickness of a single platelet ( $\sim 1$  nm) due to the presence of vitrified water on their surfaces. A close inspection of the honeycomb structures formed by 5% w/v Na-montmorillonite and 20 mM salt (Fig. 3 (b)) reveals that the average length of the branches is larger than the average lateral size (450 nm) of the Na-montmorillonite platelets. A magnified image of this sample is provided in Fig. 4 (a) which clearly shows that many of the branches have holes on their surfaces. This indicates that the platelets on each branch are connected in overlapping coin (OC) configurations, as predicted by Jonsson *et. al.* using Monte Carlo simulations in a system of clay platelets at low salt concentration [52, 53]. In the OC configuration, the positive edge of a platelet attaches to the negative basal surface near the edge of another platelet in a parallel fashion, thereby forming longer sheets (branches of the network) through attractive bonds (Fig. 4(b)). The positive edges of two such sheets (the branches) attach to the negative faces of a third sheet comprising platelets which are also in OC configurations. Such attachments lead to the formation of an attractive network-junction of three branches as indicated in Fig. 4. We note here that such honeycomb-like network formation is not very dominant in the case of the sample with 10 mM salt (a magnified image is shown in Fig. S7 of the ESI†) due to the presence of high face-face repulsions.

We use the cryo-SEM micrographs to quantify the pore (void) size distributions, porosity and branch thicknesses of all the gels studied in this work. Porosity is defined as a ratio of the total void area to the total area of the 2D projection of the gel structure. The image analysis tools used here and the details of the calculation of the porosity and network branch thickness are discussed in Section A, and in Figs. S8 and S9 of the ESI†. It is to be noted that the pore sizes measured here are smaller than the actual sizes due to the presence of

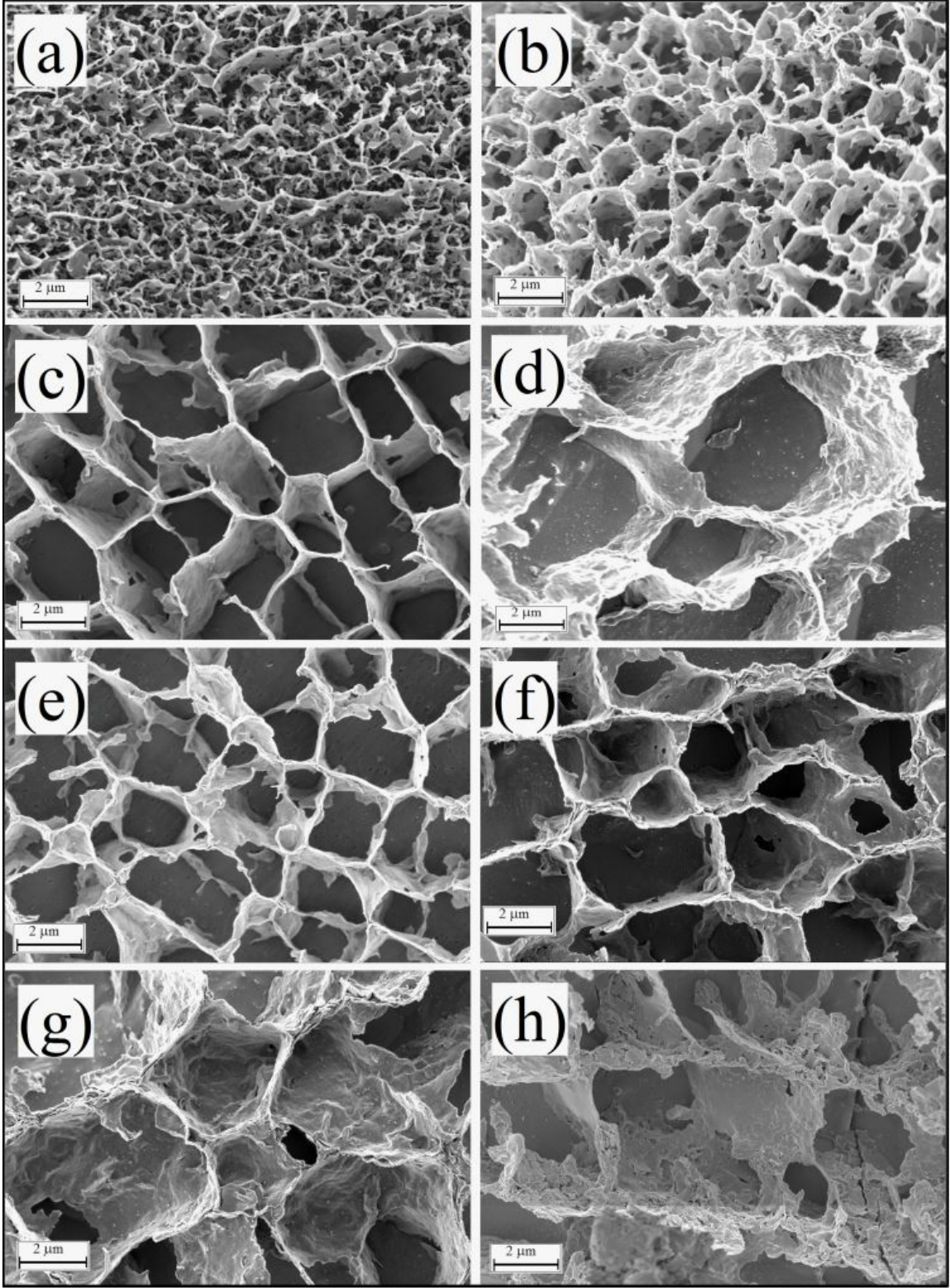


FIG. 3: Representative micrographs obtained using cryo-SEM for 5% w/v Na-montmorillonite dispersions with  $C_s = 10$  mM (a), 20 mM (b), 50 mM (c), 100 mM (d), 150 mM (e), 200 mM (f), 300 mM (g) and 500 mM (h). The scale bars represent 2  $\mu$ m.

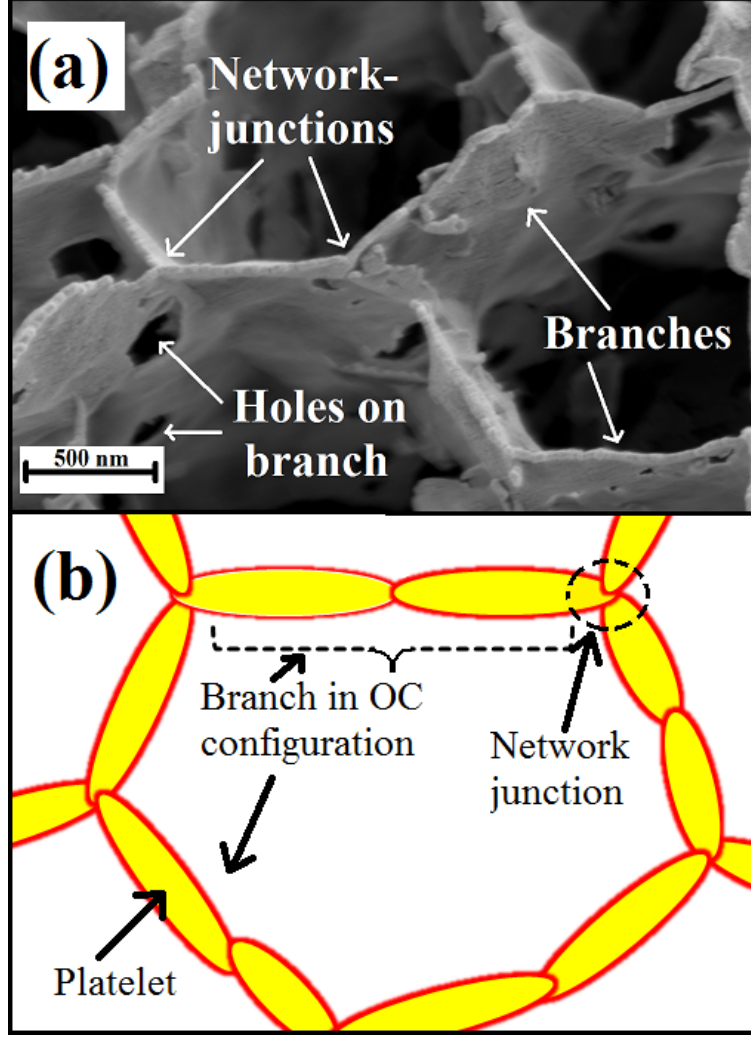


FIG. 4: (a) Magnified view of a representative micrograph obtained using cryo-SEM for 5% w/v Na-montmorillonite dispersion with  $C_s = 20$  mM. (b) Schematic depiction of the microscopic arrangement of circular platelets showing overlapping coins (OC) in dispersion in the presence of salt. The red color on the edges indicates positive charges and the yellow color on the basal surface indicates screened negative charges.

vitified water on the network. However, since the sublimation time (12 min) after fracturing the vitrified samples is same for all the dispersions, an equal sublimation-depth is expected for all the samples studied using cryo-SEM. When  $C_s$  is increased systematically upto 100 mM, the average pore size ( $\square$  in Fig. 5(a)) increases, while the porosity ( $\triangle$  in the inset of Fig. 5(a)) and branch thickness  $w$  ( $\circ$  in Fig. 5(b)) of the gels remain almost unchanged.

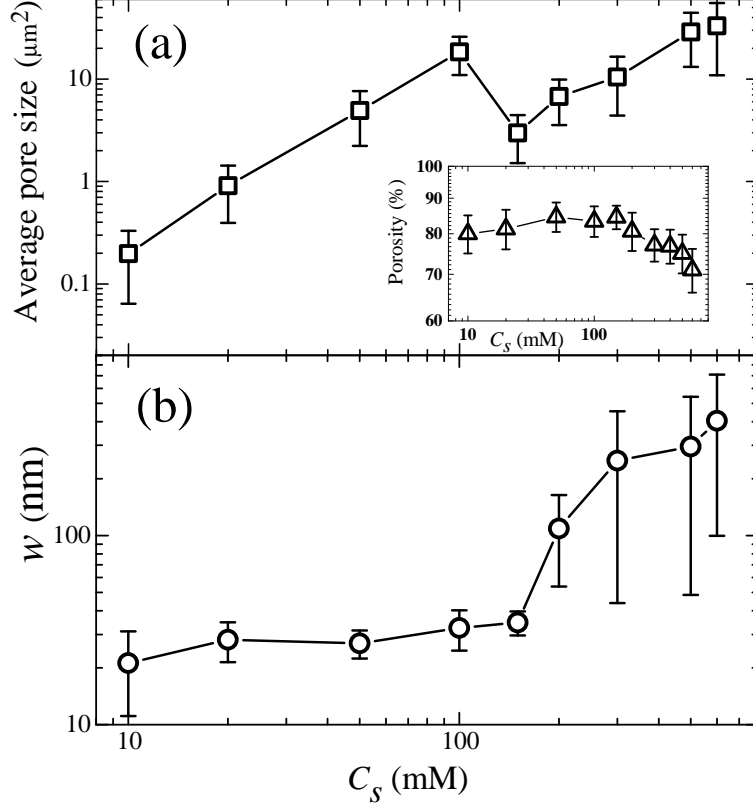


FIG. 5: (a) Plot of average pore size (□) of the gel network as a function of salt concentration  $C_s$ . Inset shows the variation of porosity (△) with  $C_s$ . (b) Plot of network-branch thickness,  $w$ , (○) as a function of  $C_s$ . The image analysis is performed using ImageJ.

It can therefore be concluded that for  $C_s \leq 100$  mM, the participation of platelets in OC configurations increases. The number of network-junctions simultaneously decreases, while the lengths of the individual branches of the network increases with  $C_s$ . This was clearly observed in Fig. 3(a), (b), (c) and (d). Interestingly, at  $C_s = 150$  mM, the average pore size (□ in Fig. 5(a)) decreases while the porosity (△ in inset of Fig. 5(a)) and  $w$  (○ in Fig. 5(b)) remain unchanged. This reduction in pore size at  $C_s = 150$  mM (Fig. 3 (e)) arises due to the participation of a substantial number of platelets in house-of-cards (HoC) configurations, apart from the OC configurations discussed earlier. In such HoC configurations, a positive edge of a platelet attaches attractively to the central negative part of the basal surface of another platelet (Fig. 6(a)). The coexistence of HoC and OC configurations can be seen in a magnified micrograph in Fig. S10 of the ESI† for a sample with  $C_s = 150$  mM. Thus, at

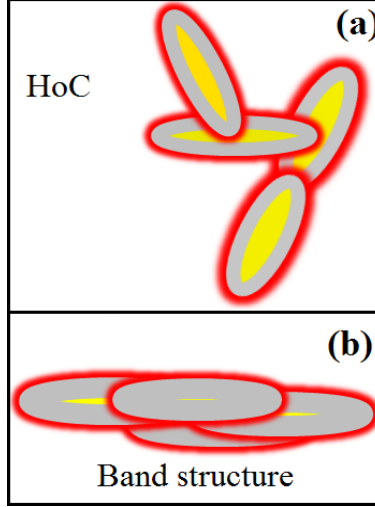


FIG. 6: Schematic depiction of (a) house-of-card (HoC) arrangement of circular platelets and (b) face-face aggregation of platelets leading to band-type structures in the dispersion in the presence of salt. The red color on the edges indicates positive charges and the yellow color on the basal surface indicates screened negative charges. The grey color indicates complete charge screening.

this salt concentration, the lengths of the network branches decrease and number of network junctions increases due to the participation of a substantial number of platelets in HoC configuration. This leads to the reduction in pore size at  $C_s = 150$  mM as observed in Fig. 5(a). It is to be noted that the coexistence of such configurations was predicted earlier in simulations of clay dispersions at high salt concentrations [53].

Since the addition of salt in the dispersing medium leads to a decrease in the Debye screening length, the spillover of negative potential from the basal surface onto the positive edges of platelets decreases with increase in salt concentration [19–21]. The effective potentials on the edges of the platelets are expected to be positive at  $C_s = 10$  mM. This leads to the formation of a gel network at this salt concentration as seen in Fig. 3(a). With increasing  $C_s$ , the magnitude of the effective positive potentials on the platelet edges increases until the long-range effects of the negative charges of the basal surface becomes negligible due to screening. As a result, the number of attractive bonds and their strengths in OC and HoC configurations increase with  $C_s$  (Fig. 3(a), (b), (c), (d) and (e)). This contributes to the growing  $G'_{pl}$  and  $\sigma_y$  of the gels upto  $C_s = 150$  mM (Fig. 2).

At  $C_s > 150$  mM, the average pore size ( $\square$  in Fig. 5(a)) and  $w$  ( $\circ$  in Fig. 5(b)) increase with increasing  $C_s$ . This was clearly observed in Fig. 3(f), (g) and (h). The total void space simultaneously decreases slightly ( $\triangle$  in the inset of Fig. 5(a)). These features, and a close inspection of the micrographs (a representative magnified image of the sample Fig. 3(f) is shown in Fig. S11, ESI $\dagger$ ), reveal that due to the considerable screening of negative charges on the basal surfaces, the face-face aggregation process due to van der Waals attractions becomes dominant under very high salt conditions [52]. Such parallel aggregation of platelets for low clay and high salt concentrations was also observed indirectly using ultrasound attenuation spectroscopy in our earlier study [48]. The face-face aggregation occurs very randomly and leads to elongated and thicker branches known as band structures (Fig. 6(b)) [54–56]. These band-type branches further connect at their ends and eventually form a kinetically arrested network characterized by a honeycomb structure. This can be seen in Fig. 3(e),(f),(g). Incomplete network formation is also observed at very high salt concentrations, e.g. at  $C_s = 500$  mM (Fig. 3(h)) and 600 mM (Fig. S12, ESI $\dagger$ ) due to the strong face-face aggregations of a considerable fraction of clay platelets.

The observed decrease in  $G'_{pl}$  and  $\sigma_y$  in Fig. 2 when  $C_s$  is increased beyond 150 mM can be attributed to the considerable increase in the pore sizes and thicknesses of the network branches which is observed in Fig. 5. In this salt concentration regime, the excluded volume due to the basal charge repulsions decreases substantially with increasing  $C_s$ . In addition, the strength of the attraction between the branches of the network also increases. As a result, applied strains promote irreversible aggregation of the thick branches. This process can lead to a higher pore size, larger branch thickness and decreasing network connectivity with increases  $C_s$ , leading to the observed decrease in  $G'_{pl}$  and  $\sigma_y$ . Such coagulation of network branches under stress can lead to the collapse of the gel network, with the yielding happening at lower  $\gamma$  values as the network branches become increasingly thicker.

We verify the stability of the gels under gravity by measuring the total vibration current ( $I_{TVI}$ ) using a sedimentation setup described in section II C. Fig. 7 shows the variation of  $I_{TVI}$  with observation time  $t_s$ , measured for 5% w/v Na-montmorillonite gels for a  $C_s$  range between 0 mM and 800 mM. The dispersion with no added salt ( $\nabla$  in Fig. 7) is highly stable under gravity due to the kinetic arrest of the constituent clay platelets. Surprisingly, we find no change in  $I_{TVI}$  values measured over two weeks for samples with  $C_s \leq 300$  mM ( $\diamond$  and

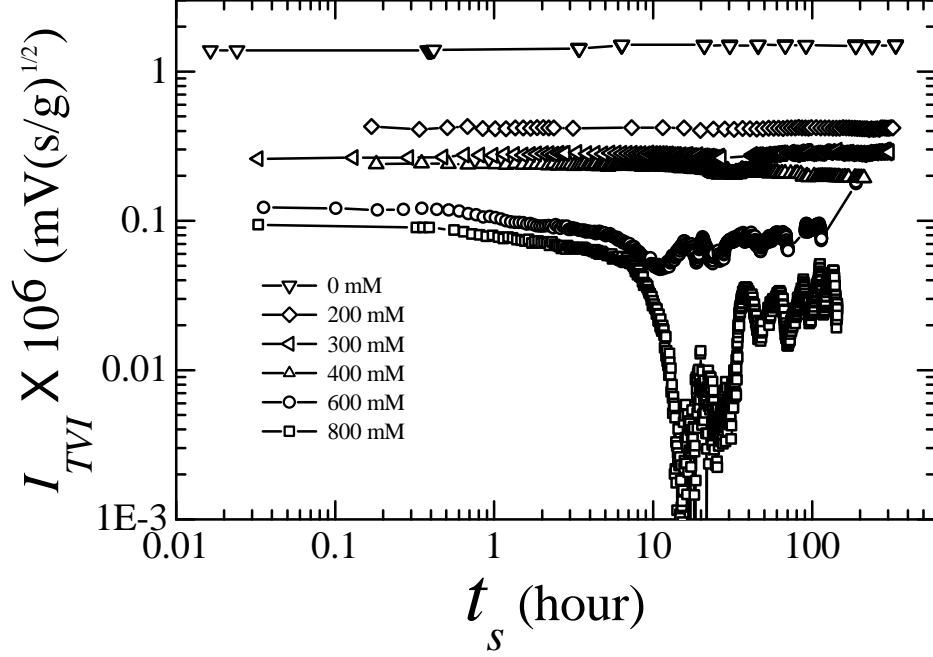


FIG. 7: Evolution of total vibration current ( $I_{TVI}$ ), normalized by the ultrasound pressure gradient, in a sedimentation setup (Fig. S6, ESI†) with observation time  $t_s$ . Here,  $t_s = 0$  is defined as the time when the stirring of the sample is stopped inside the sedimentation setup. The samples are 5% w/v Na-montmorillonite with  $C_s = 0$  mM ( $\nabla$ ), 200 mM ( $\diamond$ ), 300 mM ( $\triangleleft$ ), 400 mM ( $\triangle$ ), 600 mM ( $\circ$ ) and 800 mM ( $\square$ ).

$\triangleleft$  in Fig. 7). This indicates that the gels observed in Fig. 3(a)-Fig. 3(g) are highly stable under gravity. The sample with  $C_s = 400$  mM ( $\triangle$  in Fig. 7) exhibits a small decrease in  $I_{TVI}$  after  $t_s = 20$  hours. The dispersions with  $C_s > 400$  mM ( $\circ$  and  $\square$  in Fig. 7) show irregular oscillations with observation time  $t_s$  due to the intermittent collapse of the gel structures. As a result of the large pore sizes and thick network branches of these samples (Fig. 3 (h) and Fig. 5), the weight of the branches exceeds the local yield stress of the network, resulting in the observed gel collapse.

#### IV. CONCLUSIONS

In this article, we present our results on the influence of NaCl on the microstructures, viscoelasticity, yielding and stability of Na-montmorillonite gels at a clay concentration, 5%



$w/v$ , at which the dispersion is expected to exhibit a glassy phase in the absence of salt [48]. Microscopic observations using cryogenic scanning electronic microscopy (cryo-SEM) reveal that at low salt concentrations, the clay platelets form longer sheet structures (the network branches) through attractive overlapping coin (OC) configurations predicted in a simulation study recently [52]. These sheets (branches) join at their ends to form crosslinked ribbons (network-junctions), giving rise to honeycomb-like network structures (Fig. 3 (a), (b), (c)). Interestingly, we find that platelet participation in the OC configurations in the network-branch increases with increase in salt concentration in the range of 10-100 mM. This leads to higher pore sizes without any change in the branch thickness  $w$  of the gels (Fig. 5). With further increase of  $C_s$  upto 150 mM, the thickness of the network branches remains unchanged but the pore size of the gels decreases with  $C_s$  due to the participation of a substantial number of clay platelets in the HoC configurations, besides the usual OC configurations (Fig. 3(d)). Such a coexistence of OC and HoC at higher salt concentration was also predicted in an earlier simulation study [53]. Our rheological measurements (Fig. 2) further suggest that strength of the attractive bonds due to such platelet configurations increases with increasing  $C_s$  upto a value of 150 mM.

At  $C_s > 150$  mM, the van der Waals attraction between platelets becomes dominant due to the high screening of the basal negative charges by the  $\text{Na}^+$  ions. Under these conditions, the platelets coagulate in a face-to-face orientation randomly, leading to the formation of elongated structures known as ‘band-type structures’ that have been predicted in the literature ([54, 56]). These elongated bands further connect at their ends, with the emergence of kinetically arrested honeycomb structures (Fig. 3(e), (f), (g)). The pore sizes and branch thicknesses  $w$  of the gel networks increase with  $C_s$  due to the increase in the face-face bond formation of the platelets (Fig. 5). The strength of the gels decreases with  $C_s$  (Fig. 2) in this salt concentration regime due to a decrease in the repulsive excluded volume and a simultaneous increase in the attraction between the branches of gel network. This leads to the collapse of the gels under applied strains. It is also seen, using systematic electroacoustic measurements, that the gels exhibit considerable stability under gravity upto  $C_s = 300$  mM (Fig. 7). At  $C_s > 300$  mM, the gels become unstable due to irreversible branch coagulation, with the gel network eventually collapsing under gravity.

In conclusion, the present study elucidates the link between the bulk rheological and stability behaviors of natural Na-montmorillonite gels and their underlying microscopic struc-



tures. Apart from the significant importance of this study for various rheological applications of Na-montmorillonite, we believe that the results presented here will facilitate our understanding of the dispersion behavior of other smectite clays such as Laponite and Kaolinite in the presence of salt. Since soil is composed of natural smectites, our results are also extremely useful in the understanding of many geophysical phenomena such as landslides, and the formation of quicksand and river deltas.

## V. ACKNOWLEDGMENT

We thank Mr. A. Dhasan and Mr. K. M. Yatheendran for their help with cryo-SEM imaging.

## FOOT NOTE:

‡Electronic supplementary information (ESI) available: SEM micrograph of Na-montmorillonite platelets (Fig. S1), lateral size distribution of Na-montmorillonite platelets (Fig. S2), variation of pH of 5% w/v Na-montmorillonite dispersion with salt concentration  $C_s$  (Fig. S3), experimental protocol of rheological measurements and variation of elastic modulus,  $G'$ , and viscous modulus,  $G''$ , during shear melting process (Fig. S4), evolution of  $G'$  and  $G''$  with age,  $t_w$  (Fig. S5), experimental setup for monitoring sedimentation stability of clay dispersions (Fig. S6), a magnified cryo-SEM micrograph of 5% w/v Na-montmorillonite with  $C_s = 10$  mM (Fig. S7), analysis method of cryo-SEM images using ImageJ (Section A), a 2D projected binary form of a representative cryo-SEM micrograph (Fig. S8), pore size distribution of a 5% w/v Na-montmorillonite gel with  $C_s = 20$  mM (Fig. S9), and magnified cryo-SEM micrographs of 5% w/v Na-montmorillonite samples with  $C_s = 150$  mM (Fig. S10), 300 mM (Fig. S11) and 600 mM (Fig. S12). See DOI: \*\*\*\*\*

- 
- [1] S. Abend and G. Lagaly, *Applied Clay Science*, 2000, **16**, 201 – 227.
  - [2] S. Jabbari-Farouji, H. Tanaka, G. H. Wegdam and D. Bonn, *Phys. Rev. E*, 2008, **78**, 061405.
  - [3] R. Bandyopadhyay, D. Liang, H. Yardimci, D. A. Sessoms, M. A. Borthwick, S. G. J. Mochrie, J. L. Harden and R. L. Leheny, *Phys. Rev. Lett.*, 2004, **93**, 228302.

- [4] A. S. Negi and C. O. Osuji, *Journal of Rheology (1978-present)*, 2010, **54**, 943–958.
- [5] D. Saha, Y. M. Joshi and R. Bandyopadhyay, *Soft Matter*, 2014, **10**, 3292–3300.
- [6] V. Tudisca, M. A. Ricci, R. Angelini and B. Ruzicka, *RSC Adv.*, 2012, **2**, 11111–11116.
- [7] D. Saha, R. Bandyopadhyay and Y. M. Joshi, *Langmuir*, 2015, **31**, 3012–3020.
- [8] J. Fossum, *The European Physical Journal Special Topics*, 2012, **204**, 41–56.
- [9] L. Bailey, H. N. W. Lekkerkerker and G. C. Maitland, *Soft Matter*, 2015, **11**, 222–236.
- [10] S. C. Glotzer and M. J. Solomon, *Nat Mater*, 2007, **6**, 557 – 562.
- [11] B. Ruzicka and E. Zaccarelli, *Soft Matter*, 2011, **7**, 1268–1286.
- [12] R. Barbara, Z. Emanuela, Z. Laura, A. Roberta, S. Michael, M. Abdellatif, N. Theyencheri and S. Francesco, *Nature Materials*, 2011, **10**, 56 – 60.
- [13] E. Paineau, A. Philippe, K. Antonova, I. Bihannic, P. Davidson, I. Dozov, J. Gabriel, M. Imperor-Clerc, P. Levitz, F. Meneau and L. Michot, *Liquid Crystals Reviews*, 2013, **1**, 110–126.
- [14] F. Uddin, *Metallurgical and Materials Transactions A*, 2008, **39**, 2804–2814.
- [15] H. H. Murray, *Applied Clay Science*, 2000, **17**, 207 – 221.
- [16] C. Viseras, C. Aguzzi, P. Cerezo and A. Lopez-Galindo, *Applied Clay Science*, 2007, **36**, 37 – 50.
- [17] Y. Liu, M. Zhu, X. Liu, W. Zhang, B. Sun, Y. Chen and H.-J. P. Adler, *Polymer*, 2006, **47**, 1 – 5.
- [18] F. Bergaya and G. Lagaly, in *Handbook of Clay Science*, ed. F. Bergaya and G. Lagaly, Elsevier, 2013, vol. 5, pp. 1 – 19.
- [19] R. Secor and C. Radke, *Journal of Colloid and Interface Science*, 1985, **103**, 237 – 244.
- [20] E. C. Y. Yan and K. B. Eisenthal, *The Journal of Physical Chemistry B*, 1999, **103**, 6056–6060.
- [21] D. Zhou, A. I. Abdel-Fattah and A. A. Keller, *Environmental Science & Technology*, 2012, **46**, 7520–7526.
- [22] E. Verwey and J. Overbeek, *Theory of Stability of Lyophobic Colloids*, Elsevier: Amsterdam, Netherlands, 1948.
- [23] H. Tanaka, J. Meunier and D. Bonn, *Phys. Rev. E*, 2004, **69**, 031404.
- [24] K. Norrish, *Discuss. Faraday Soc.*, 1954, **18**, 120–134.
- [25] F. A. Bowles, *Science*, 1968, **159**, 1236–1237.
- [26] H. van Olphen, *John Wiley and Sons Inc.: New York*, 1977, **53**, 230–230.

- [27] L. J. Michot, I. Bihannic, F. Thomas, B. S. Lartiges, Y. Waldvogel, C. Caillet, J. Thieme, S. S. Funari and P. Levitz, *Langmuir*, 2013, **29**, 3500–3510.
- [28] J. Duran, M. Ramos-Tejada, F. Arroyo and F. Gonzalez-Caballero, *Journal of Colloid and Interface Science*, 2000, **229**, 107 – 117.
- [29] G. Lagaly and S. Ziesmer, *Advances in Colloid and Interface Science*, 2003, **100?âĈĤâĤIJ102**, 105 – 128.
- [30] G. Broughton and L. Squires, *The Journal of Physical Chemistry*, 1935, **40**, 1041–1053.
- [31] H. van Olphen, *Journal of Colloid Science*, 1964, **19**, 313 – 322.
- [32] P.-I. Au and Y.-K. Leong, *Colloids and Surfaces A: Physicochemical and Engineering Aspects*, 2013, **436**, 530 – 541.
- [33] H. Kimura, M. Sakurai, T. Sugiyama, A. Tsuchida, T. Okubo and T. Masuko, *Rheologica Acta*, 2011, **50**, 159–168.
- [34] P. B. Laxton and J. C. Berg, *Journal of Colloid and Interface Science*, 2006, **296**, 749 – 755.
- [35] M. Dijkstra, J. P. Hansen and P. Madden, *Phys. Rev. Lett.*, 1995, **75**, 2236–2239.
- [36] J. Wierzechos, C. Ascaso, M. T. Garcia-Gonzalez and E. Kozak, *Clays and Clay Minerals*, 1992, **40**, 230–236.
- [37] M. S. Zbik, W. N. Martens, R. L. Frost, Y.-F. Song, Y.-M. Chen and J.-H. Chen, *Langmuir*, 2008, **24**, 8954–8958.
- [38] H. Tanaka, S. Jabbari-Farouji, J. Meunier and D. Bonn, *Phys. Rev. E*, 2005, **71**, 021402.
- [39] R. Angelini, E. Zaccarelli, F. A. de Melo Marques, M. Sztucki, A. Fluerașu, G. Ruocco and B. Ruzicka, *Nature communications*, 2014, **5**, year.
- [40] A. Thill, S. Moustier, J.-M. Garnier, C. Estournel, J.-J. Naudin and J.-Y. Bottero, *Continental Shelf Research*, 2001, **21**, 2127 – 2140.
- [41] A. Khaldoun, E. Eiser, G. Wegdam and D. Bonn, *Nature*, 2005, **437**, 635–635.
- [42] *Nanocor Inc.*, *Technical data sheet*, G-105, (Last accessed on 22nd February 2015).
- [43] H. V. Olphen, *Journal of Colloid Science*, 1962, **17**, 660 – 667.
- [44] Y. Zheng and A. Zaoui, *Solid State Ionics*, 2011, **203**, 80 – 85.
- [45] J. D. F. Ramsay, S. W. Swanton and J. Bunce, *J. Chem. Soc., Faraday Trans.*, 1990, **86**, 3919–3926.
- [46] A. Cadene, S. Durand-Vidal, P. Turq and J. Brendle, *Journal of Colloid and Interface Science*, 2005, **285**, 719 – 730.

- [47] S. Ali and R. Bandyopadhyay, *Langmuir*, 2013, **29**, 12663–12669.
- [48] S. Ali and R. Bandyopadhyay, *Applied Clay Science*, 2015, **114**, 85–92.
- [49] A. S. Dukhin and P. J. Goetz, *Characterization of Liquids, Nano- and Microparticulates, and Porous Bodies using Ultrasound*, Elsevier: New York, 2010.
- [50] K. Miyazaki, H. M. Wyss, D. A. Weitz and D. R. Reichman, *EPL (Europhysics Letters)*, 2006, **75**, 915.
- [51] M. Laurati, S. U. Egelhaaf and G. Petekidis, *Journal of Rheology (1978-present)*, 2011, **55**, 673–706.
- [52] B. Jonsson, C. Labbez and B. Cabane, *Langmuir*, 2008, **24**, 11406–11413.
- [53] M. Delhorme, B. Jonsson and C. Labbez, *Soft Matter*, 2012, **8**, 9691–9704.
- [54] A. Weiss and R. Frank, *Naturforsch*, 1961, **16**, 141–142.
- [55] T. Permien and G. Lagaly, *Applied Clay Science*, 1994, **9**, 251 – 263.
- [56] P. F. Luckham and S. Rossi, *Advances in Colloid and Interface Science*, 1999, **82**, 43 – 92.